HardwareX 19 (2024) e00569

Contents lists available at ScienceDirect

HardwareX

journal homepage: www.elsevier.com/locate/ohx

Hardware article

A customizable digital holographic microscope

Claudia Ravasio [a,*], Luca Teruzzi [b], Mirko Siano [b], Llorenç Cremonesi [a], Bruno Paroli [b], Marco A.C. Potenza [b,c]

[a] Earth and Environmental Sciences Department, University of Milano-Bicocca, Milan, Italy
[b] Department of Physics, University of Milan, Milan, Italy
[c] Interdisciplinary Centre for Nanostructured Materials and Interfaces (C.I.Ma.I.Na.) and Department of Physics, University of Milan, Milan, Italy

ARTICLE INFO

Keywords:
Digital holography
Optics
Microscopy
Mineral dust
Ice cores

ABSTRACT

We propose a compact, portable, and low-cost holographic microscope designed for the characterization of micrometric particles suspended in a liquid. This system is built around a commercial optical microscope by substituting its illumination source (a light-emitting diode) with a collimated laser beam. Similarly, a quartz flow cell replaces the microscope glass slide using a 3D-printed custom mount. With the hardware presented in this paper, the holographic imaging of the electromagnetic fields emitted by the particles that intercept the laser beam achieves a resolution close to that of optical microscopes but with a greater depth of field. Several morphological and optical features can be extracted from the holograms, including particle projected section, aspect ratio, and extinction cross-section. Additionally, we introduce a remote system control that enables users to process the acquired holograms on a remote computational device. This work provides a comprehensive description of the methodology of image processing in holographic microscopy and a series of validation measurements conducted using calibrated particles. This technique is suitable for the characterization of airborne particles found in snow, firn, and ice; here we report experimental results obtained from Alpine ice cores.

Specifications table

Hardware name	μHolo
Subject area	• Digital Holography • Mineral dust • Cryosphere
Hardware type	• Imaging and scattering tools • Measuring physical properties
Closest commercial analog	Digital holography microscope
Open source license	CC-BY 4.0
Cost of hardware	2700 €
Source file repository	https://data.mendeley.com/datasets/k38sfd28py/2

* Corresponding author.
E-mail address: claudia.ravasio@unimib.it (C. Ravasio).

https://doi.org/10.1016/j.ohx.2024.e00569
Received 7 February 2024; Received in revised form 20 May 2024; Accepted 9 August 2024
Available online 13 August 2024

1. Hardware in context

Digital holography (DH) is a robust and versatile imaging technique that suits a wide range of applications, from the examination of micro-components [1] to dynamic three-dimensional tracking systems [2]. It is also used in the medical field, such as in diagnostics and cardiology [3]. In addition, DH also demonstrates its effectiveness in aerosol analysis, e.g. for particle counting and morphological characterization [4], even on particles embedded in snow or ice [5]. Its applications further span industrial electronics, entertainment, virtual reality, and cyber–physical security, where it has found numerous innovative uses [6]. The advantages of the DH methods over conventional microscopy are many. It provides a non-contact approach, preserving the samples, and gives quantitative information, e.g. particle shape [5,7,8], cross-sectional area [5,7], particle refractive index [9], 3D position in space [10,11], and how fast the particles move [12]. This is thanks to the acquisition of both amplitude and phase of light reflected or scattered from an object [13], while conventional optical microscopes capture the intensity and little information about the phase. Another advantage over conventional optical microscopes is the ability to achieve an extended depth of field (DOF). In a brightfield microscope, the DOF diminishes rapidly, necessitating mechanical refocusing to examine a large volume. In contrast, the holographic image is 'focused' through numerical processing after it is acquired. This eliminates the need for mechanical moving parts and can be done in real-time or as a post-processing step, depending on the computational resources available. Additionally, DH enables the simultaneous imaging of multiple objects in different focal planes. This enhances its versatility and effectiveness in various scientific and industrial applications. DH can be performed using different configurations, i.e., in-line [14–16], following the original holographic scheme proposed by Gabor [17], or off-axis, where the source is split into two beams before it reaches the sample: one of these beams propagates through the optical system undisturbed by the object creating an external reference wave [18–20]. On the one hand, in-line holography improves the temporal stability of the quantitative phase imaging system and ensures a large Field Of View (FOV), and on the other hand, off-axis techniques have the advantage of handling twin-image artifacts [21].

DH microscope research has already reached the stage of commercialization (e.g. https://www.lynceetec.com/digital-holography/, https://phiab.com/holomonitor/holographic-microscopy/, [8,22–25]). On-chip microscopes [23,24] employ digital holography with partially coherent source LED illumination. Their advantage is the large FOV which corresponds to the whole detector area. The low temporal and spatial coherence of LEDs can further suppress extraneous fringes and speckles relative to a diode laser. However, this configuration has usually a small sensor with a small pixel size ($<3\,\mu m$) that yields fewer gray-scale levels and may degrade the image quality because it results in a lower dynamic range and signal-to-noise ratio. This can be overcome by the use of a point source in-line holographic microscopy [8,22–25]. In this configuration a spherical reference incident wave emanates from a pinhole, illuminating the sample at a distance D from the point source, and producing a magnification of the sample that depends on the distance between the detector and the point source, and D. Despite the straightforward setup of this approach, with no lenses to introduce optical aberrations, the detector must be placed far from the point source and the scatterers. The result is that, with its limited surface, the detector collects only light at small scattering angles while missing information relevant to the optical properties of the objects.

In this work, we propose an instrument using already available tools also in a common laboratory. Creating a DH microscope is indeed relatively straightforward. We present an implementation of in-line DH microscope that is portable and simple to align, by replacing the non-coherent source in a conventional bright-field microscope with a coherent laser beam directed at the specimen and magnified by an objective lens. Therefore, it is like a module that can be easily added to a device that already exists [22]. In the case a microscope is not already available among laboratory equipment, the cost of the presented hardware is 2700 €, we will discuss cheaper alternatives below. This adaptation provides good-quality images with good sharpness and minimum speckles. In this study, we exploit the technique to measure the properties of micron-sized particles that are stored in alpine snow and ice cores, which can be analyzed in liquid after melting. DH effectively manages sample polydispersity, making it ideal for analyzing dust suspensions from ice cores and snow samples, especially under conditions of strong dilution. This approach enables direct measurements of particle shadow, i.e. the cross-sectional area (csa) of the particle, and the extinction cross-section (C_{ext}). Obtaining this information is crucial for the essential single-scattering characteristics required by the radiative transfer models [26–28]. Although portable and low-cost DH solutions of ranging complexity have recently been reported [23,25,29], critically important details necessary for their realization in a laboratory are mostly disclosed, especially when we are analyzing a flow sample in a continuous mode. When dealing with melted water samples from ice cores, up to 40 000 images can be collected for each sample (usually this takes no more than 40 min for each measurement). With the proposed method, we can analyze each image, discard the empty ones, and collect statistical information about the csa of the particle and the (C_{ext}) of the sample [5].

2. Hardware description

We modified a commercial microscope (BRESSER Erudit DLX 40-1000x Microscope, Fig. 1) by replacing its white light-emitting diode (LED) with a pigtailed diode laser (Thorlabs LP642-SF20, 20 mW, wavelength λ =642 nm, 60 mA, Fig. 1, a) coupled with a commercial collimator (F110FC-633 Fiber Collimation, Thorlabs, Fig. 1, b) for precise beam control. Moreover, the system has been equipped with a quartz flow cell (Starna Linear Flow cell, 5 × 0.2 mm channel thickness, Fig. 1, c). Within this configuration, the collimated laser beam transilluminates the sample. A custom assembly realized by additive manufacturing (3D-printed , Fig. 1, d) allows us to install the flow cell on the platform where microscope slides are placed. The cell is tilted by an angle of about 10° from the plane perpendicular to the laser optical axis to prevent multiple reflections that would cause detrimental stray light interference fringes. Since we wanted to control the flow rate, a peristaltic pump is used to deliver a steady stream of $<2\,\mu L\ s^{-1}$ to the illuminated region using a peristaltic pump. The small fraction of light diffracted by the sample object superimposes to the (almost unchanged)

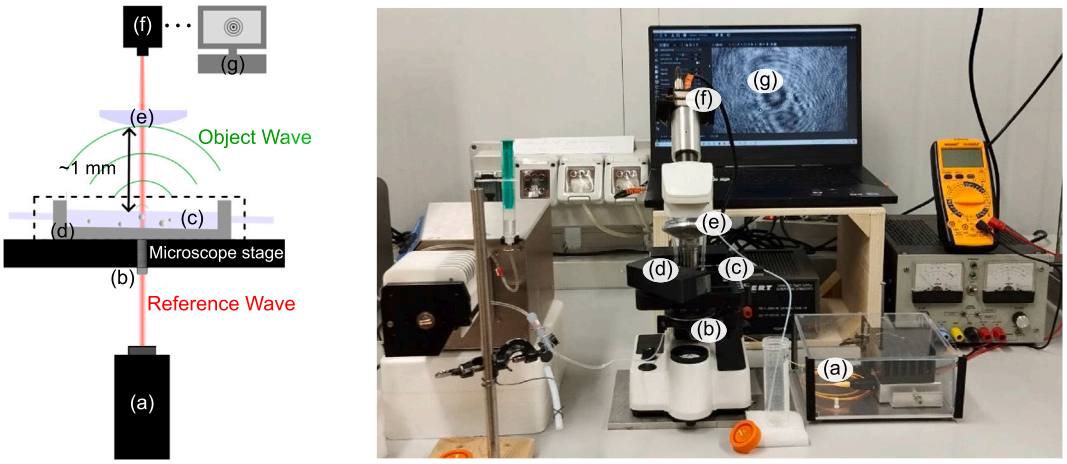

Fig. 1. Left: a sketch of the in-line DH technique integrated on a commercial microscope. Right: photo of the commercial bright-field microscope with the digital holography technique integrated. A pigtailed diode laser (a) coupled to a collimator (b) illuminates a flow cell (c) through which water-suspended particles are driven. The cell is inserted in a custom holder (d) A 20× microscope objective (e) magnifies the hologram pattern, which is then recorded by a CMOS sensor (f). The information is collected and stored by a laptop (g). Drawing not to scale. (For interpretation of the references to color in this figure legend, the reader is referred to the web version of this article.)

intense transmitted beam to produce a holographic interference pattern. In this way, the Gabor self-referenced scheme is realized, which guarantees superior stability [16]. The holographic interference pattern is collected in the far field of the diffracted light. The hologram is magnified 20× by a microscope objective (Edmund DIN 20X, Numerical Aperture 0.40, Fig. 1, e) onto the plane of a CMOS detector (IDS camera GV-5260CP-M-GL, 1920 × 1200, 5.86 µm pixel size, Fig. 1, f). The recording system is the camera, whose position defines a plane conjugate to the observation plane: no image is formed onto the camera if there is no object in the observation plane. The recorded information is not an image but rather the interference pattern of the scattered/diffracted wave with the reference wave magnified by the microscope objective. Anyway, we kept the terminology for collecting the interference pattern, as usually intended in holography. The image acquisition can be operated in real-time through a laptop (Fig. 1, g). The hardware works regardless of the choice of the optical microscope or the camera. The spectral response of the camera adopted here is not perfectly matched to the red laser wavelength. A green laser could in principle be the best choice, although no relevant drawbacks are there in using red.

With our implementation, DH can be easily operated by a large user community without a specific optical laboratory, using already available tools. Thanks to the collimated laser beam of our setup, it is easier to reconstruct holograms recorded at any distance from the object, thanks to the afocal property of the beam. The magnification given by the objective lens applies to the whole scattering volume in the cell and does not depend on the axial position. Compared with the brightfield microscope, we have a similar lateral resolution. Limitations may come from the Numerical Aperture (NA) of the collection optics or the Nyquist frequency of the sensor pixel array, which we verified is not the case. Therefore we can characterize the lateral resolution as:

$$R_x = \frac{\lambda}{2\mathrm{NA}} = 0.8\,\mu\mathrm{m}. \tag{1}$$

The main advantages of this setup are:

- not requiring an accurate alignment
- afocal property of the beam
- compatible with established in-line DH methods
- suitable for sample polydispersity and continuous flow analyses

2.1. Image acquisition

The camera is controlled by the proprietary software *IDS peak 2.5*. However, many openly available interfaces can be used as an alternative. For example, *PyLabLib cam-control* is a universal software for camera control and image acquisition openly available on GitHub. Detailed documentation is provided at https://github.com/AlexShkarin/pyLabLib-cam-control. Both the exposure time and the frame rate can be adjusted with the user interface; in our case, we set them to 0.05 ms and 50 fps, respectively. Since several images are collected with no particles in the field of view, a filtering algorithm takes care of removing any image characterized by an intensity variance below a given threshold. This operation can be easily performed in real-time, or even in post-processing mode. The threshold is determined based on the following equation:

$$\frac{\sigma^2_{I_{\mathrm{raw}}} - \sigma^2_{I_{\mathrm{bkg}}}}{\sigma^2_{I_{\mathrm{raw}}}} \cdot 100 > t \quad , \tag{2}$$

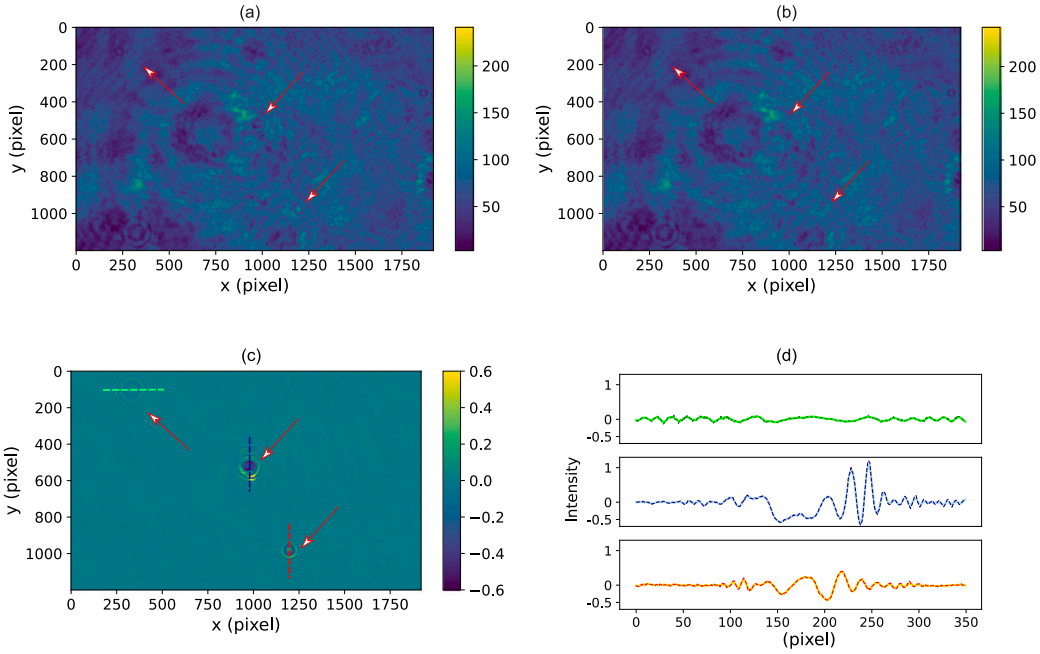

Fig. 2. Example of the pre-processing procedure described in the text obtained with data from dust in meltwater from ice cores. (a) The *raw image*, which contains three holograms indicated by arrows. The intensity of each hologram pattern depends on the physical properties of the particles. (b) The *background image*, i.e. the input of the sensor in the absence of particles. (c) The *contrast hologram*, obtained from images (a) and (b) via Eq. (3). (d) Hologram intensity along horizontal or vertical dashed lines in (c).

where σ^2 is the variance and the threshold value t depends on the thickness and the refractive index of the objects under study. I_{raw} indicates the raw image and I_{bkg} is the background intensity distribution, which is the intensity distribution without any object. The background intensity profile I_{bkg} must be continuously monitored. In principle, this would require knowing when there are no objects in the field of view, that is, knowing the threshold itself. We overcome this issue by averaging 20 raw holograms. Thanks to the strong dilution of the samples, this is enough to guarantee that most of them are recorded without any particles. In the case of more concentrated samples, a proper evaluation of the minimum number of images can be easily performed to guarantee the absence of persistent interference patterns in the background image. In the present work, we set $t = 0.1\%$ since the difference between an image with and without objects was almost negligible, as shown in Fig. 2, c-d. However, for larger objects on the order of millimeters, this threshold could increase up to 5%.

Before reconstructing the holograms, pre-processing is applied to the raw images to compensate for the unavoidable intensity inhomogeneities across the laser beam. We then introduce the *contrast hologram* as the result of the following normalization [4,30,31]:

$$H_{\text{contr}} = \frac{I_{\text{raw}} - I_{\text{bkg}}}{I_{\text{bkg}}} \quad . \tag{3}$$

By its definition, the contrast hologram is immune to intensity fluctuations due to the laser beam or the liquid flowing into the cell. It provides an interference pattern close to the ideal hologram originated by a uniform plane wave without any disturbance. In Fig. 2 we show an example of a raw image (a), the corresponding background image (b), the contrast hologram (c), and the hologram intensities along the horizontal or vertical axis in the hologram plane (d).

2.2. Remote control

Here we introduce a solution that can be easily implemented with a Raspberry Pi (Raspberry Pi3, model 3B, 1 GB RAM). We chose the Raspberry Pi3 because it is relatively cheap and has more RAM and onboard storage compared to most development boards with similar features, although it requires a full-fledged operating system. These characteristics make it suitable for performing memory-expensive tasks such as image processing and the variance filtering described in Eq. (2). In addition, while microcontrollers often have a limited number of I/O pins, Raspberry Pi3 offers a wider range of GPIO (General Purpose Input/Output) pins along with additional interfaces such as USB external storage devices. Thanks to the built-in support for both Wi-Fi and Bluetooth connectivity, it is possible to control the system from any mobile device, e.g. a phone or tablet by using the open-source RaspController application (openly available at https://play.google.com/store/apps/details?id=it.Ettore.raspcontroller&gl=US&pli=1). Python libraries such as

Table 1
Listing of the available commands to remotely control the Raspberry Pi3 and monitor data acquisition.

Command	GPIO number	Action	Logic state
Start camera connection	14	Collect camera information (such as sensor exposure time and black level) and starts the acquisition of background images.	GPIO 14: logic 1 GPIO 15: logic 0 GPIO 17: logic 0 GPIO 23: logic 0
Start acquisition	15	Start data acquisition, with a frame rate ranging from 1 to 3 fps.	GPIO 14: logic 1 GPIO 15: logic 1 GPIO 17: logic 0 GPIO 23: logic 0
Status pin	17	Interrupt data acquisition; the device waits for a further command, allowing to start a new measurement, (GPIO 15) or to close the current session.	GPIO 14: logic 1 GPIO 15: logic 0 GPIO 17: logic 1 GPIO 23: logic 0
Abort running and quit	23	Stop the application and safely remove the USB device.	GPIO 14: logic 0 GPIO 15: logic 0 GPIO 17: logic 0 GPIO 23: logic 1

GPIOzero are available and make the use easy enough to implement dedicated interfaces (https://gpiozero.readthedocs.io/en/stable/). By using RaspAP (openly available at https://raspap.com/), a feature-rich wireless router software working on many popular Debian-based devices, the instrument acts as a Wi-Fi router to which the user can connect remotely. RaspAP only works on *Lite* releases of the Raspbian operative system (both 32-bit and 64-bit), *i.e.* without any graphical user interface.

Here we introduce a general workflow to remotely control the camera, shown in Fig. 3. First, the Raspberry Pi connects to the camera (Fig. 3, 1) and simultaneously recognizes any external storage device. The communication between the Raspberry Pi3 and the IDS camera occurs through the GigE RJ45 interface connector, with a transmission speed of about 1.00 Gbps. The commands for connecting the IDS camera to the microcontroller through the ethernet port and to start, stop, or pause measurements are implemented through specific Python functions described in Section 3 and can be run by acting through RaspController on the GPIO channels. The available commands and their corresponding GPIO number are summarized in Table 1. All GPIOs are initially configured with a low voltage state (logical 0), except for GPIO 17, which is set to a high voltage state (logical 1). This particular GPIO is used to indicate the pin status (0 = deactivate remote control, 1 = activate remote control). The acquisition of the background (Fig. 3, 2) starts by switching the GPIO 14 to *on* state. After acquiring the images needed to obtain the background, the measurement can be started by switching the GPIO 15 to *on*. As described above, the system checks for the presence of an object within the frame by calculating the variance (Fig. 3, 3). Alternatively, selected holograms can be reconstructed in real-time. In our case, we can set the acquisition frame rate up to ~3 images per second, mainly limited by RAM capacity. Switching the GPIO 17 *off* (Fig. 3, 4), the measurement is stopped. The procedure can be halted through GPIO 23.

2.3. Holographic reconstruction

We now move on to describing the algorithm that reconstructs the hologram. The numerical reconstruction of the holograms follows well established methods [13,16,31–34], and takes advantage of the open-source package HoloPy (https://github.com/manoharan-lab/holopy, [35]). The first step involves the particle localization. We find the center of the particle by cross-correlating the object within the hologram intensity distribution and the scattering solution K for a spherical object [36,37], defined as:

$$K = 2\frac{S(0)}{kz'}\cos\left(\frac{k}{2z'}R^2 + \frac{\pi}{2}\right)g(\theta) \quad , \tag{4}$$

where $S(0)$ is the dimensionless scattering amplitude, z' is the focal position, k is the wavenumber, and $g(\theta)$ is the form factor, the characteristic function of the interference pattern accounting for the intensity damping as the scattering angle increases. $R = \sqrt{\xi^2 + \eta^2}$, and (ξ, η) are the coordinates of the hologram plane, as in Fig. 4. In the case of a non-square contrast hologram image, the distance matrix must be adjusted accordingly, taking the form of $R = \sqrt{h\xi^2 + \eta^2}$, where h defines the aspect ratio of the camera (16:10 in this work). The outcome is a matrix containing sharply defined peaks. These centers directly correspond to the particle positions within the observation plane. Upon retrieving the scatterers positions, the original image is cropped to remove areas without fringes, to reduce the computational load. In the case of multiple objects, the image is separated into multiple sub-images. A threshold is set to exclude any hologram too close to the image edges: only image sections ranging from 150 × 150 to 400 × 400 pixels are retained. Since Eq. (4) depends on z' and on the particle size, for which we used an average value, the resulting cropped images may not be perfectly centered. However, it is important to find the center of the hologram accurately. To this aim, we use a circular Hough-based holographic feature detection algorithm [38], implemented in the Holopy package, to further refine the center location on the cropped images.

The overall imaging concept of in-line digital holography and object reconstruction is outlined in Fig. 4. The diffracted field $E_s(x', y')$ at position (x', y') on the image plane at z' is related to $H_{contr}(\xi, \eta)$ on the hologram plane through the Rayleigh-Sommerfeld

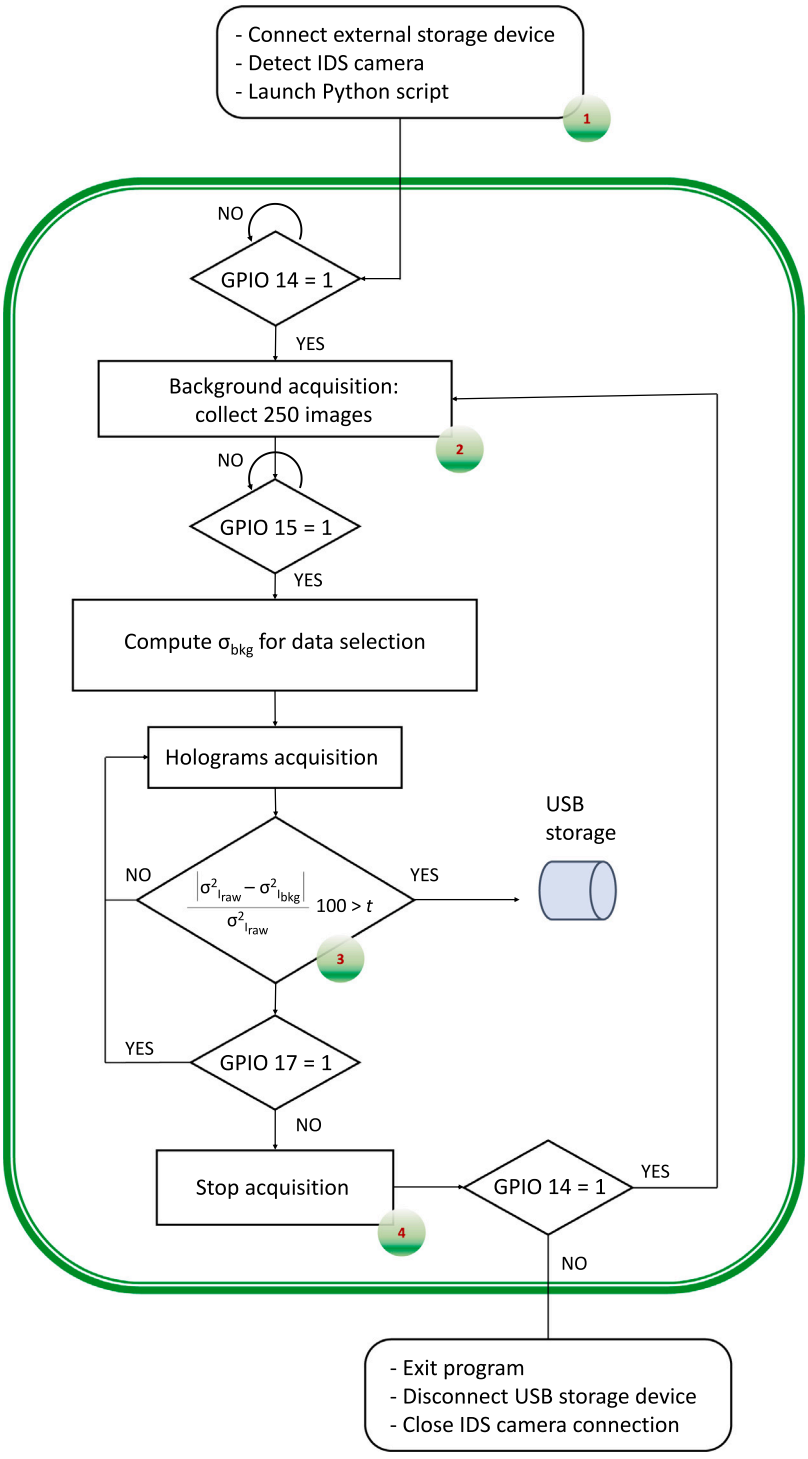

Fig. 3. A sketch of the workflow implemented for the general remote software.

diffraction formula [39]:

$$E_s(x', y') = \frac{E_0}{i\lambda} \iint H_{\text{contr}}(\xi, \eta, z = 0) \frac{e^{ik\rho}}{\rho} \mathrm{d}\xi \mathrm{d}\eta \quad . \tag{5}$$

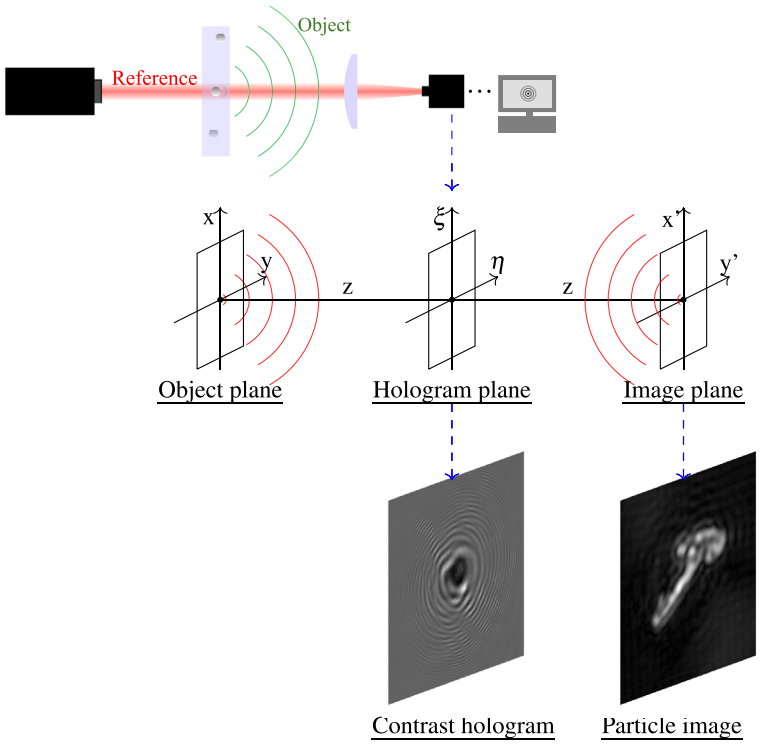

Fig. 4. (top) A collimated laser beam impinges on a cell through which samples are flown. We plot in red the reference wave, while in green the object wave. A microscope objective is used to image the magnified hologram pattern onto a sensor. (center) System of coordinates and distances involved in the image reconstruction process. (bottom) Example of a contrast hologram $H_{\text{contr}}(\xi,\eta)$ of a dust aggregate and the corresponding reconstructed image in the plane (x',y'). (For interpretation of the references to color in this figure legend, the reader is referred to the web version of this article.)

Here λ is the light wavelength, E_0 is the reference incident (constant) wave, ξ and η are the coordinates in the hologram plane (as depicted in Fig. 4) and the integrals extend over the entire hologram plane. We introduce

$$\rho = \sqrt{(\xi - x')^2 + (\eta - y')^2 + z'^2} \quad , \tag{6}$$

as the distance between a point $P_0(\xi,\eta,z=0)$ on the hologram plane and $P_1(x',y',z')$ on the image plane. We omitted the obliquity factors $\cos\theta$ since the solid angle of the sensor is small. Different realizations of this diffraction integral exist, which are comprehensively detailed in [4,31,32]. We use the propagation function implemented in the Holopy package, based on the *angular spectrum method*. The Rayleigh-Sommerfel diffraction formula (Eq. (5)) is equivalent to the convolution between the contrasted hologram $H_{\text{contr}}(\xi,\eta)$ and the impulse response $G(\xi,\eta,x',y') = \frac{1}{i\lambda}\frac{e^{ik\rho}}{\rho}$:

$$E_s(x',y') = E_0 \cdot [H_{\text{contr}}(\xi,\eta) \circledast G(\xi,\eta,x',y')] \tag{7}$$

where the symbol $\circledast$ denotes the convolution operator. By the convolution theorem, we can calculate Eq. (7) by first Fourier transforming H_{contr}, then multiplying by the Fourier transform of G, and taking an inverse Fourier transform of this product:

$$E_s(x',y') = \mathcal{F}^{-1}\left\{\mathcal{F}\{H_{\text{contr}}\}\cdot\mathcal{F}\{G\}\right\}, \tag{8}$$

Therefore, the diffraction formula (Eq. (5)) can be calculated with three Fourier transforms; a fast FFT algorithm can be used. In practice, in our configuration we propagate the field over a distance vector spanning from 50 to 550 µm with 5 µm steps. According to the literature, the exact focal position z' is extracted by looking for an abrupt increase in the amplitude of $|E_s(x',y')|^2$ along the optical axis [40,41]. The procedure is comparable to inspecting a sample using an optical microscope and physically shifting the specimen to achieve a focused image. Fig. 5 depicts a sketch of this process: the particle at z_1 (green line in Fig. 5) is out of focus at z_2, and vice-versa.

In Fig. 6, we summarize the steps to retrieve geometrical information about the particle. From the contrast hologram (Fig. 6, a), the particle shadow is obtained from the intensity distribution $|E_s(x',y')|^2$ reconstructed in the image plane (Fig. 6, b). Finally, we create a binary image (Fig. 6, c) by imposing a threshold of 20% of the maximum of $|E_s(x',y')|^2$. This threshold is established during the calibration test, as detailed in Section 7.2. This approach allows us to reconstruct the geometric *csa* and, for example, calculate the aspect ratio (*ar*) from the major and minor axes (Fig. 6, d). These are the Euclidean lengths of the sides of a bounding rectangle around each particle.

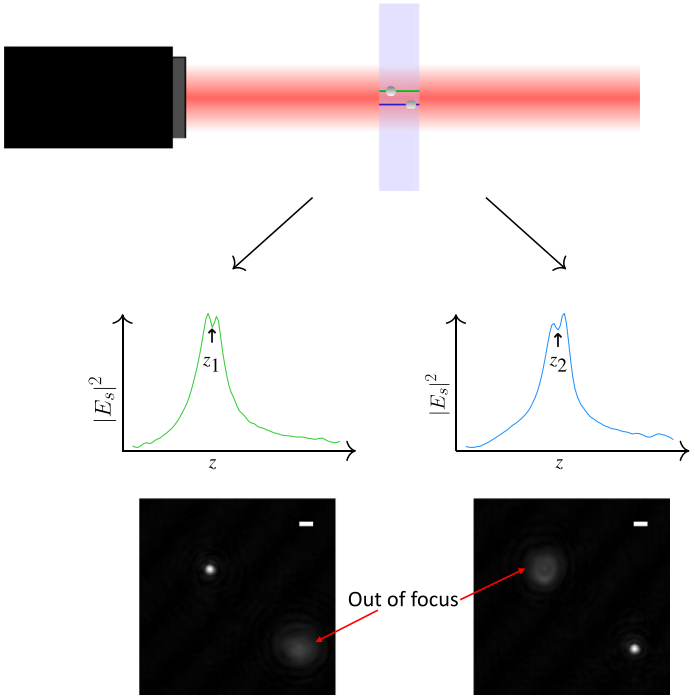

Fig. 5. (top) Example of the reconstruction of two holograms from polystyrene particles at different focal depths, z_1 and z_2. (center) Intensity profile of $|E_s|^2$ along the longitudinal axis centered on the respective (ξ, η) particle positions. (bottom) Images of polystyrene particles reconstructed from each hologram. The white bar on the top-right corner of each image is set to 2 µm. (For interpretation of the references to color in this figure legend, the reader is referred to the web version of this article.)

Another parameter of utmost importance is the extinction cross-section, defined as the power removed by the particle divided by the impinging intensity. This can be obtained by simply comparing the signals collected by the camera in the presence and absence of the object by integrating the contrast hologram (by Eq. (3)) [42]. Let us consider a single object illuminated by a collimated laser beam incident on a sensor. Ideally, the resulting hologram acquired by the sensor oscillates symmetrically about zero. If no particles are detected, the sensor instead acquires a hologram where all pixels are equal to zero [43]. Now consider some centered square portions over the interference pattern of the contrasted hologram, marked as A–D in Fig. 7, a. If we perform an integration over these square portions, we obtain an oscillatory trend curve, as shown in Fig. 7, b, where the corresponding points marked are aligned with the same labels in Fig. 7, a. Since the image is discretized in pixels, this opration can be written in a Python code as:

```
f = np.zeros(L)
for i in range(L):
    f[i] = np.sum(I_cont[L-i:L+i, L-i:L+i]) * Delta**2
```

i.e., explicitly,

$$f = \Delta^2 \sum_{j,k=L-i}^{L+i} \texttt{I\_cont}_{jk} \tag{9}$$

where $L = N/2$ is the position of the center of the hologram of size N, `Delta` $= \Delta$ is the pixel size, and $i = 0, \ldots, L-1$. f has therefore the unit of an area, in terms of Δ^2. From this we define $\theta = \arctan(\Delta \cdot i / z')$. As shown in Fig. 7(b), $f(\theta)$ increases from 0 to a maximum value, then oscillates and finally decays to an asymptote depending on the nature of the scatterer. The curve vanishes asymptotically in the case of non-absorbing objects (because the absorption coefficient (C_{abs}) is null). For absorbing objects the curve will simply approach C_{abs}. By computing the upper and lower envelopes of $f(\theta)$ and determining the average trend, an extrapolation to $\theta = 0$ typically yields C_{ext} within an error of about 10%. By extrapolating $f(\theta)$ for large θ (greater than 20°) provides the C_{abs} [7]. Unfortunately, this angular size is difficult to achieve in practice, and cannot be implemented in the current version of our setup. The angular size is strictly dependent on the shape factor of the particle, i.e., its size. One way to overcome the difficulty of having such a large angular size of the sensor could be to place the image and the object planes at a smaller distance so that the number of oscillations within the taper is greater. However, it should be considered that the hologram is marred by speckles and obscured by fringes due to other surfaces and particles along the optical train. This method only works for a single particle: if the captured image contains even two nearest holograms, the C_{ext} can be obtained with a good approximation, unlike C_{abs}.

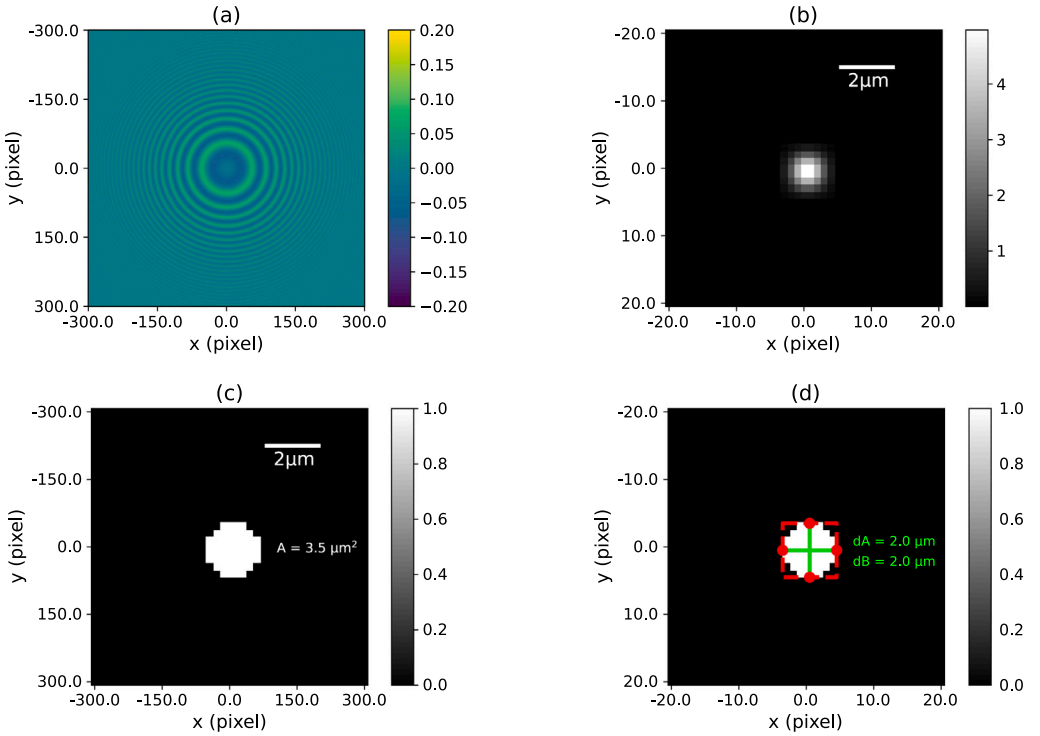

Fig. 6. Examples of processing data. (a) The contrast hologram of a not-absorbing particle with $d = 2\,\mu m$, and $m = 1.19$. The hologram is simulated using the Lorenz-Mie formalism using the open-source package HoloPy (detector shape = 601 × 601 pixel, pixel size = 0.26 μm, $\lambda = 0.633\,\mu m$, $z = 300\,\mu m$). (b) By propagating the field to the focal plane, we obtain the particle shadow. (c) By setting a threshold in amplitude, we can obtain the cross-sectional area (*csa*). Finally in (d), by computing a bounding rectangle around the particle (red dashed lines) we obtain the value of the cross-sectional height and width (green lines) and their ratio (*ar*). (For interpretation of the references to color in this figure legend, the reader is referred to the web version of this article.)

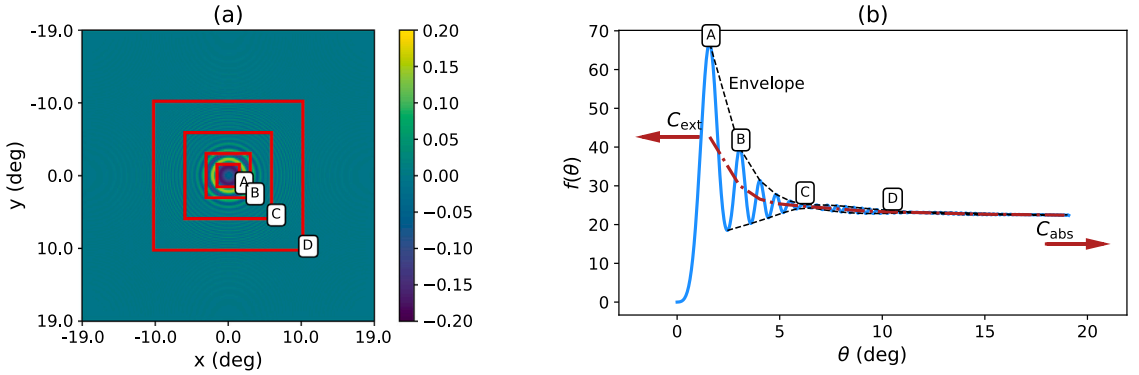

Fig. 7. (a) A contrast hologram with some square segments marked as A-D, matching points labeled similarly in the plot of the $f(\theta)$ function in (b). This curve results from integrating the contrast hologram of an absorbing particle with $d = 5\,\mu m$, $m = 1.19 + i0.1$, $C_{ext} = 43\,\mu m^2$ and $C_{abs} = 22\,\mu m^2$. We can derive the value of C_{ext} from the minimum angle value on the trend curve, indicated by the red arrow, and estimate C_{abs} from the maximum angle. The hologram is simulated using the open-source package HoloPy (detector shape = 1201 × 1201 pixel, pixel size = 0.26 μm, $\lambda = 0.633\,\mu m$, $z = 450\,\mu m$).

3. Design files

The design files are available from the project's repository (https://data.mendeley.com/datasets/k38sfd28py/2). The following is a lists for the hardware components, which are are summarized in Table 2, and here shortly described:

- eyepiece_camera_adapter.f3d: contains the drawing of the eyepiece adapter. It can be opened and edited with the openly available program Fusion3D and many CAD programs. Usually the eyepiece - camera adapter is included with the microscope. Otherwise, a custom aluminum assembly or a 3D-printed adapter can be made according to these specifications.
- flow_cell_adapter.f3d: file containing the scheme for the 3D printing of the custom flow cell adapter.

Table 2
Design files.

Design filename	File type	License	Location
eyepiece_camera_adapter.f3d	Fusion3D	CC BY 4.0	data_mendeley
flow_cell_adapter.f3d	Fusion3D	CC BY 4.0	data_mendeley
flow_cell_box.f3d	Fusion3D	CC BY 4.0	data_mendeley

Table 3
Main 3D printing parameters.

Parameter	Value	Parameter	Value
Extruder width	0.4 mm	Nozzle temperature	200 °C
Layer height	0.15 mm	Plate temperature	50 °C
Filling pattern	rectilinear	Default speed	1800 mm/min
Filling percentage	22%	Perimeter speed	1080 mm/min
Filament diameter	1.75 mm	Top/bottom speed	1440 mm/min
Material type	PLA	**Material type**	PLA

- flow_cell_box.f3d: file containing the drawing of the cell box used to avoid signal fluctuations due to straylight sources.

The main 3D printing parameters for manufacturing these components are listed in Table 3.

The software files consist of two repositories. The PyCamera_control project allows acquiring images remotely, as explained in Section 2.2. The HoloSoft package is based on the algorithm explained in Sections 2.1 and 2.3. All files are listed in Table 4, and here shortly described:

```
PyCamera_control
├── README.md
├── AUTHORS
├── VERSION
├── LICENSE
├── setup
│   ├── requirements.txt
│   └── setup.py
├── methods
│   ├── IDS_camera.py
│   ├── acquisition.py
│   └── utils.py
├── main
│   ├── PyCamera.py
│   └── start_system.sh
└── manual
    ├── OS_notes.pdf
    └── manual.pdf
```

- PyCamera_control: Python project used to remotely control the image acquisition from the camera. It includes Python scripts and the instructions for both installing the software and running the remote acquisition project. The main file is PyCamera.py, and the dependency can be installed by the requirement file (requirements.txt). The basic instructions for getting started can be found in the readme file and the code is open source on GitHub (https://github.com/OpticaLab/PyHoloCamera) and on the project's repository (data_mendeley). Here we provide a brief description of the methods and the file structure:
  - PyCamera.py: main script for remote image acquisition and setting of the main physical and operational parameters;
  - start_system.py: bash shell script which controls the Raspberry Pi - CMOS camera connection, the external storage device identification and enables the Raspberry Pi GPIO control sequence;
  - IDS_camera.py: Python script to set some parameters of the IDS CMOS sensor (such as the exposure time);
  - acquisition.py: Python code for the remote camera control. After the CMOS detector connection and setting, background images are acquired and their variance and standard deviation are evaluated. Afterward, the hologram acquisition starts: if the image contains at least one hologram it is saved in the specified directory, otherwise it is ignored and the acquisition process continues. This selection is based on the variance filter as described above (Eq. (2)). All the information and useful parameters are stored in a dedicated log file.
  - setup.py: installs required Python dependencies from the requirements text file.
  - utils.py: contains supplementary functions to start the preliminary background image acquisition and the variance threshold.

Table 4
Software files.

Software filename	File type	Open source license	Location of the file
PyCamera.py	Python	GNU v3.0	GitHub
setup.py	Python	GNU v3.0	GitHub
IDS_camera.py	Python	GNU v3.0	GitHub
offline_acquisition.py	Python	GNU v3.0	GitHub
utils.py	Python	GNU v3.0	GitHub
system_setup.sh	Bash	GNU v3.0	GitHub
tutorial.py	Jupyter Notebook	GNU v3.0	GitHub
function_CEXT.py	Python	GNU v3.0	GitHub
function_SHAPE.py	Python	GNU v3.0	GitHub
function_FIND_CENTERS.py	Python	GNU v3.0	GitHub
ImgCorrect.py	Python	GNU v3.0	GitHub
main_dust.py	Python	GNU v3.0	GitHub
_launch.sh	Bash	GNU v3.0	GitHub

- HoloSoft: Python package used to analyze the raw images as described in Sections 2.1 and 2.3. The package is available on GitHub (https://github.com/OpticaLab/Holosoft), and on the project's repository (data_mendeley). By running the setup.py file, the package is installed in the correct environmental path. We refer the reader to the readme file for further installation details. Holosoft takes advantage of well-validated routines from the Holopy repository (https://github.com/manoharan-lab/holopy). Although Holopy provides a well-structured tutorial for the analysis of single images, there is a lack of information on how to work in a continuous mode, e.g. how to automatically detect the focal position of the particles. This is a crucial task for a flow analysis, where hundreds of images are acquired, with or without particles in the field of view. In the HoloSoft package, we have created an automatic routine that first delays the empty image and then reconstructs the particles to obtain their *csa*. Finally, we include the computation of the C_{ext}, which is not available in the Holopy repository. The results are automatically saved to a *txt* file. Outliers due to noise are efficiently removed. We have created a tutorial that explains the routine for a single image. Here, a brief description of the methods and the file structure:

```
HoloSoft
├ README.md
├ AUTHORS
├ VERSION
├ LICENSE
├ requirements.txt
├ setup.py
├ _launch.sh
├ analysis
│  ├ ImgCorrect.py
│  └ main_dust.py
└ src
   ├ __init__.py
   ├ function_CEXT.py
   ├ function_SHAPE.py
   ├ function_FIND_CENTERS.py
   └ function_utilities.py
```

  - _launch.sh: bash shell script to run the main script with argparse (command-line options, arguments);
  - requirements: install automatically the required Python packages;
  - main_dust.py: main script for the image reconstruction;
  - ImgCorrect: main script for deleting empty raw images;
  - tutorial.ipynb: Jupyter notebook tutorial to learn how the main script works through simple interactive steps. An example image is included.

4. Bill of materials summary

This section presents the parts and materials bought to build this experimental setup, and a complete list is shown in Table 5. The costs are to be considered without labor. The total price is 2700 €. With the alternative components, the price goes down to 900 €.

5. Assembling instructions

A summary of the setup instructions is provided.

Table 5
Bill of materials used for this hardware.

Designator	Component	Cost (€)	Alternative component	Cost (€)
Laser Diode	LP642-SF20 - 642 nm, 20 mW, A Pin Code, SM Fiber-Pigtailed Laser Diode, FC/PC. Source: laser_thorlab	596.22	L252 - Compact Laser Module with USB Connector, 639 nm, 4.5 mW. Source: alt_laser_thorlab	155
Laser Diode Driver	LD1255R - 250 mA Precision Constant Current Laser Driver. Source: laser_driver_thorlab	164.13	Integrated with the laser Diode. Source: alt_laser_thorlab	–
Collimator	Thorlabs - F110FC-633 - 633 nm, f = 6.17 mm, NA = 0.38 FC/PC Fiber Collimation Pkg. Source: collimator	161.30	–	161.30
Flow cell	Starna Linear Flow cell, inlet/outlet tubes parallel to the light beam, 48-Q-0.2, Quartz. Source: starnacells	320.94	–	320.94
Flow cell adapter	Flow-cell adapter. 3D printer, PLA	0.51	–	0.51
Flow cell box	Flow-cell box custom assembly. 3D printer, PLA	1.06	–	1.06
Objective lens	Edmund DIN 20X NA 0.40, Achromatic Finite Intl Standard Objective. Source: objective	140	3 objectives: 4x, 10x and 40x included with the microscope. Source: alt_microscope	–
Microscope	BRESSER Erudit DLX 40-1000x Microscope. Source: microscope	275	BRESSER Biolux NV 20x-1280x Microscope with HD USB Camera. Source: alt_microscope	170
Eyepiece - Camera adapter	Eyepiece - Camera adapter. Aluminum or PLA	–	Included with the microscope. Source: alt_microscope	–
Camera	IDS camera GV-5260CP-M-GL. starnacells. Source: camera	790	IDS camera UI-5241LE-MB Rev.1.2 Source: alt_camera. Alternatively, the camera included with the microscope. Source: alt_microscope	420 –
Camera cable	IDS IO cable Hirose HR25 all signals 5 m P. Source: camera_cable	130	–	–
Raspberry Pi (Optional)	Raspberry Pi3, model 3B, 1GB RAM. Source: raspberrypi	84.30	–	84.30

- Begin by disassembling the LED illumination system of the microscope (Fig. 8, 1).
- Fabricate the flow cell adapter using the design file from flow_cell_adapter.f3d with a 3D printer.
- Insert the flow cell into the translation stage where glass slides are commonly placed (Fig. 8, 2), and connect the inlet and outlet pipes (Fig. 8, 3).
- Realize a 3D print of the cell box (Fig. 8, 4), according to the project flow_cell_box.f3d.
- Connect the laser diode to the collimator and insert it into the flow-cell adapter under the translation stage (Fig. 8, 5).
- The file eyepiece_camera_adapter.f3d provides a custom adapter. The appropriate printing parameters are described in Table 3.
- Connect the adapter to the camera (Fig. 8, 6). The heat sink over the camera (Fig. 8, 7) reduces dark noise current and the risk of overheating during long-term continuous acquisitions, but it is not essential for the operation. Thus, it is not included among the camera accessories.
- Start the calibration process described in Section 7 (Fig. 8, 8) by flowing a known and calibrated sample into the flow cell. In our case, the inlet and outlet pipes were connected to a peristaltic pump to precisely set the flow rate. This pump is part of a suite of instruments to which the digital holographic microscope described in this paper also belongs, therefore we chose to use it. However, we point out that to flow liquid through the cell, the cheapest solution we adopted in some cases is to let the sample flow with a free-falling liquid system that can be finely tuned to set the flow rate.

6. Operation instructions

- Switch on the laser source. The laser is powered by a driver that allows fine-tuning of the supplied current. In our specific case, the current is set to 60 mA (Fig. 9, 1). The driver can be powered by any dual power source within the range 8–12 V, also including a very cheap PC power supply unit.
- Switch on the camera and connect it to the personal computer (Fig. 9, 2).
- Launch the camera control software and configure the settings: set exposure time to 0.05 ms and frame rate to 50 fps.
- Check the alignment of the objective lens and the laser source by examining the pixel intensity histogram in the software; a Gaussian profile indicates the alignment is correct (Fig. 9, 3).
- Determine the object distance z' by adjusting the microscope stage. We used a focal distance of about $300\,\mu m$.
- Flow ultrapure water into the system in an open loop configuration; make sure that no signals are recorded (blank).
- Prepare the sample and start the frame acquisition. We recommend to keep the flow rate below $2\,\mu L\ s^{-1}$. Save up to 10^4 images at a time and begin the preliminary analysis described in Section 2.1 to discard empty images (Fig. 9, 4).

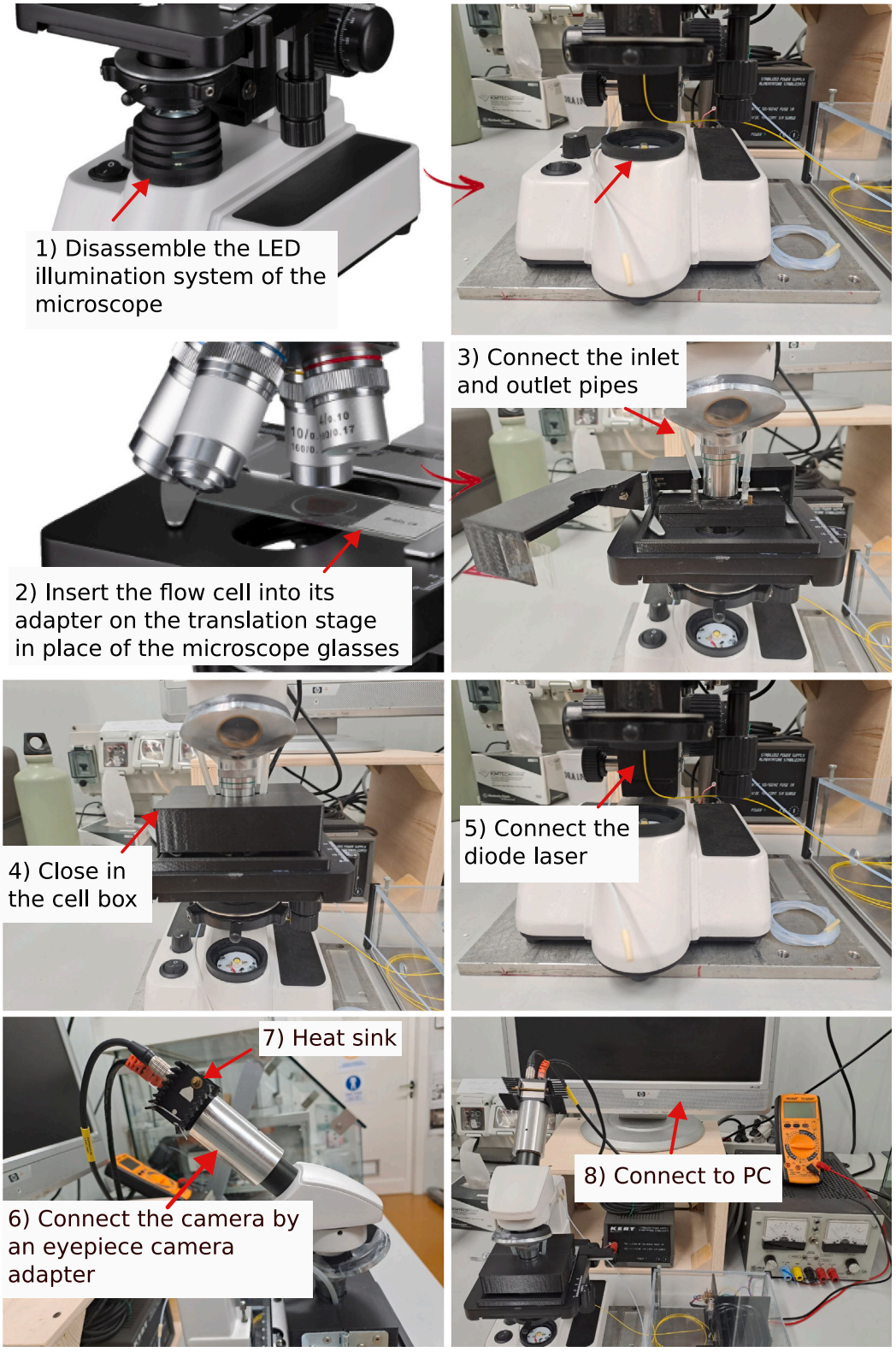

Fig. 8. Visual guide for the setup instructions in a few simple steps.

- Stop the acquisition process, refer to the tutorial from the software file “tutorial.ipynb”, and start the post-processing analysis (Section 2.3).

7. Validation and characterization

7.1. Accurate determination of the system magnification

To measure particle size correctly, it is essential to know the magnification of the system. We measure the magnification factor M of our system by tracking Near Field Speckles (NFS) generated by a random diffuser undergoing rigid translations [44]. By working in the deep near field regime [45], we establish a one-to-one relation between the speckle displacement observed on the camera Δx_{sp} and the diffuser translation Δx [46]:

$$\Delta x_{\mathrm{sp}} = \Delta x \cdot M \quad . \tag{10}$$

Notice that Eq. (10) is valid in the deep near field only, since the displacements of the diffuser would result in completely renewed speckle patterns in the far field zone [44,46].

The experimental setup is shown in Fig. 10. The diffuser (a microscope glass covered with opaque tape) is mounted onto a linear translation stage with a step $\delta x = 20\,\mu\mathrm{m}$. We place the diffuser between $500\,\mu\mathrm{m}$ and $1\,\mathrm{mm}$ out of focus to fulfill the deep near field requirements. We then acquire a sequence of NFS images (200 frames in our case) for different lateral positions of the diffuser, obtained by moving the translation stage by δx. Therefore, an image lag l corresponds to a physical displacement $\Delta x = l \cdot \delta x$ of the diffuser. Examples are reported in Fig. 11, a and b, where red circles track some groups of speckles as a reference to the eye. Finally, for any image lag l, we evaluate the speckle displacement Δx_{sp} in Eq. (10) by first extracting the position of the peak in the cross-correlation function between two subsequent images, as shown in Fig. 11, c, then by averaging the results over all possible image pairs. This yields a high accuracy in the determination of the magnification of the system thanks to the high statistics generated from the acquired speckle sequence. Results are reported in Fig. 11, d, alongside with a linear fit according to Eq. (10). The measured magnification is $M = 23.73 \pm 0.01$, where the error is determined by the fit. Using this value, we can obtain the *effective pixel size* by dividing the nominal pixel size by the magnification.

7.2. Calibration with known-sized particles

The system performance, especially the reconstruction algorithm, underwent rigorous testing with a procedure that allows us to operate the system under real conditions, i.e. with the cell and the water flowing inside. We collected several numbers of holograms using a diluted colloidal suspension of $2.1\,\mu\mathrm{m}$ polystyrene (PS) beads. We extensively employed these calibrated polymeric particles as a reference for our experimental measurements [5,47,48]. To prevent agglomeration, we immersed the diluted samples (diluted with pure water at a ratio of approximately 1 to 2500 in two steps) in an ultrasonic bath for 5 min. The measurement of C_{ext} was employed to enhance the accuracy of the *effective pixel size* within the hologram plane (ξ, η). This fine-tuning was essential to account for the variation of the pixel size due to the magnification. The csa was utilized to establish the cutoff value for the particle shadow in the reconstruction algorithm. The most suitable values for the pixel size and cutoff have been determined to be $0.25\,\mu\mathrm{m}$ and 20%, respectively. In this way, the reconstructed images allowed us to calibrate both the magnification (M = 23.44) and the resolving power from the intensity distribution at the borders, resulting in good accordance with that estimated in Section 7.1 and with Eq. (1). Fig. 12 represents the C_{ext} (a) and csa (b) distributions, which are close to their expected values. By fitting the data with a Gaussian distribution, we obtain an average of $10.72 \pm 1.46\,\mu\mathrm{m}^2$ and $3.35 \pm 0.33\,\mu\mathrm{m}$, to be compared to the expected values of $10.63\,\mu\mathrm{m}^2$ and $3.46\,\mu\mathrm{m}^2$ for the C_{ext} and area values, respectively. Theoretical values are obtained using the HoloPy package.

7.3. Mineral dust characterization

As a practical application, we present some results obtained by measuring meltwater suspensions of dust contained in the upper snow layers from the Rutor Glacier (2500 m a.s.l. - Aosta Valley, Italy), shown in Fig. 13. Alpine ice and snow samples are notable for their high dust concentrations and their susceptibility to fluctuations in climatic and environmental conditions. These samples consist primarily of mineral dust derived from the erosion of nearby mountainous regions. However, a substantial amount of mineral dust can be transported over long distances from North Africa by Saharan dust storms, which are the world’s largest source of aeolian desert dust [49]. Furthermore, the outstanding absorbing properties of carbonaceous particles and other aerosols from anthropogenic sources make their contribution to these samples significant [50]. During the melting season, there is also a considerable release of microalgae, microorganisms, and bacteria, which can produce red or green snow patches and accelerate snow loss by reducing the albedo of the snow surface in the visible wavelengths [51–53]. We observed a great number of aggregates, probably due to a melting process. Some examples are shown in Fig. 13, a and b. They are recognized due to the anomalously large dust size distribution. The algorithm can recognize single particles within the aggregate, as in Fig. 13, b. The more complex the geometry of the scatterer and the more the hologram pattern (shown on the left in Fig. 13) exhibits convoluted fringes, that reveal its shape. We point out that DH cannot detect past melting events directly. However, a proxy for such events is an increase in particle concentration, particularly in the form of aggregates. In Fig. 13, c, we show an example of a coarse particle (with principal axes $\sim 9\,\mu\mathrm{m}$, a particle radius much larger than the incident wavelength). For this type of particles, the amplitude of the scattered field is higher in the forward

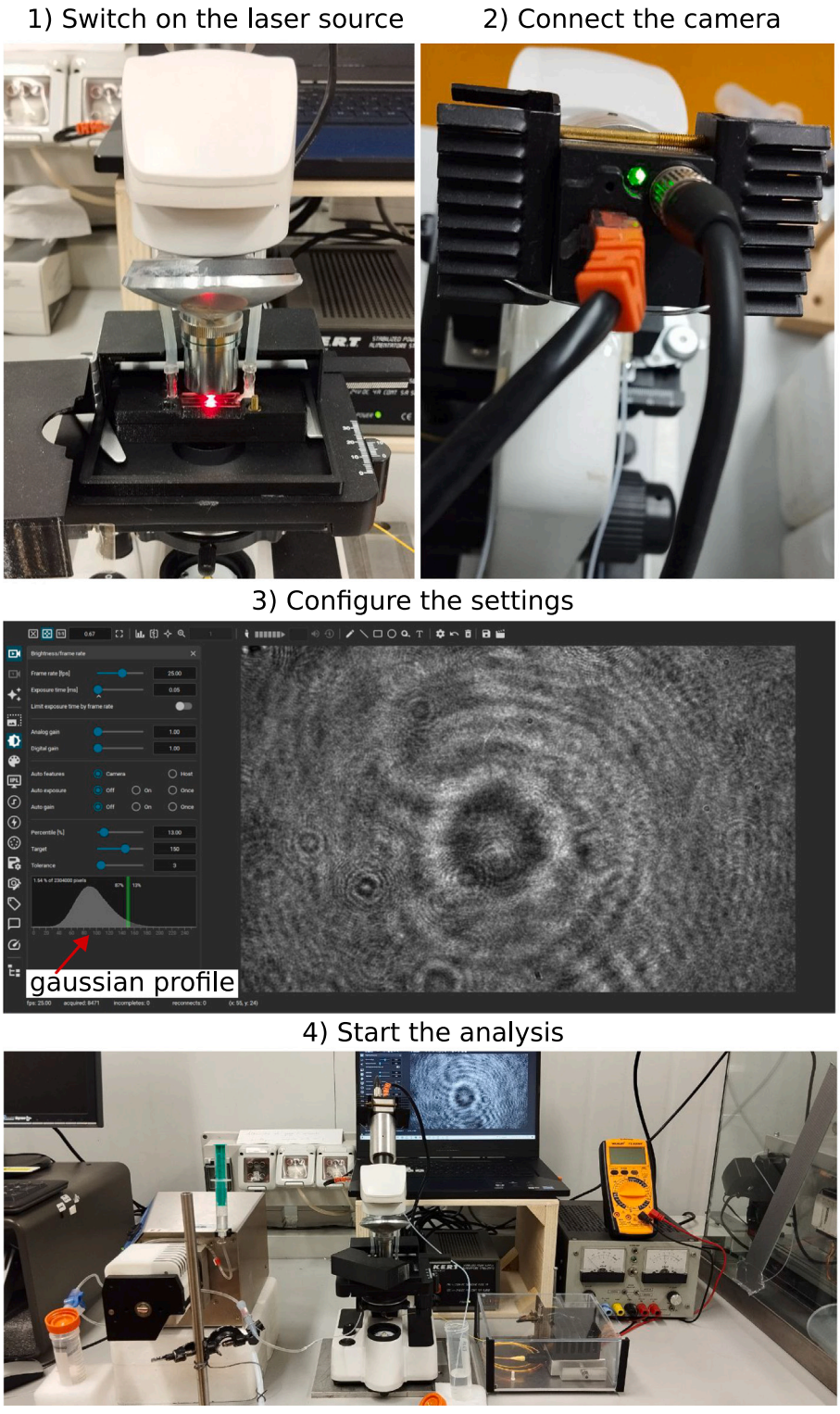

Fig. 9. Visual guide for the operation instructions in a few simple steps.

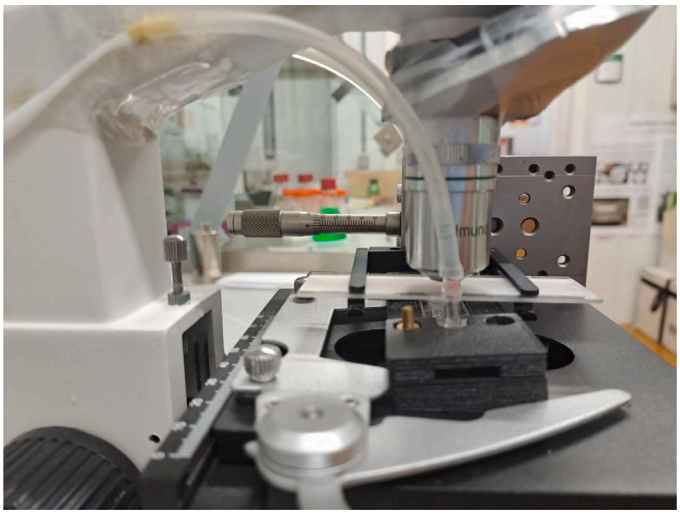

Fig. 10. Picture of the commercial bright-field microscope integrating the DH technique. The linear translation stage and the diffuser used for the accurate determination of the system magnification are also present. They are then removed during the holographic acquisitions.

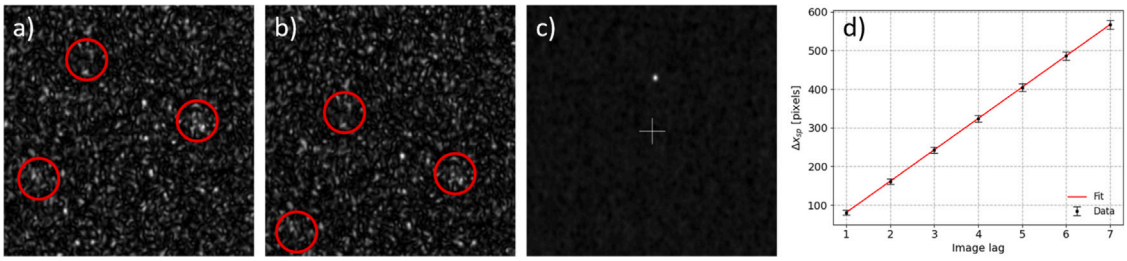

Fig. 11. Examples of near field speckle patterns for different lateral positions of the diffuser (a,b), the corresponding cross-correlation function (c), and position of the peak in the cross-correlation function for different image lags (d). Red circles in (a, b) are used to visually track groups of similar speckles. In (d), the solid line represents a linear fit according to Eq. (10). (For interpretation of the references to color in this figure legend, the reader is referred to the web version of this article.)

direction, in contrast to fine particles, whose amplitude decreases more uniformly toward the edges (shown in Fig. 13, d and e). Furthermore, in Fig. 13, c, we observe an unusual shadow shape. This peculiar phenomenon stems from the challenges associated with determining the axial position of coarse scatterers. Modeling the holograms with an exact solution (specifically, the Lorenz-Mie solution for the scattering of a plane wave by isolated spheres [36]) shows that the intensity peak along the optical axis is far from the actual location of the scatterer [54]. The plot shows not one but two maximum positions, located around the edges of the particle and separated by a local minimum, which is the right focal position. Despite this elongation in the axial direction, it is still possible to computationally determine the correct *csa* of the particles. Finally, in Fig. 13, d and e, we present samples characterized by a spherical shadow, but with notably different values of C_{ext}. This discrepancy is also evident from the respective holograms on the left. The variation in C_{ext} can be attributed to a non-isometric shape of the particle in panel (d). Using the Amsterdam Discrete Dipole Approximation (ADDA) code [55] to compute the C_{ext} of non-spherical particles (as indicated by the dotted colored line in Fig. 14), we can observe that the C_{ext} for the particle in (d) is lower than that of spherical particles modeled using Mie spheres (represented by the gray region in Fig. 14). In particular, the particle appears to be well approximated by a spheroidal shape with an optical depth less than its diameter, resulting in a thickness-to-diameter ratio (*tdr*) of about 0.6. While the particle in panel (e) is well approximated by a spherical shape.

8. Conclusions and future developments

In this paper, we introduced an affordable, compact, and transportable holographic microscope designed for the analysis of mineral dust in ice cores and snow samples. The hardware includes a coherent laser beam instead of the light-emitting-diode (LED), and a flow cell 3D-printed custom assembly instead of the microscopic glass. The result is an innovative use of a microscope to characterize micron-sized dust and a facile application of digital holography, which does not require any optics laboratory equipment. The system is very robust to mechanical misalignments and permits rapid digital reconstruction of the images of

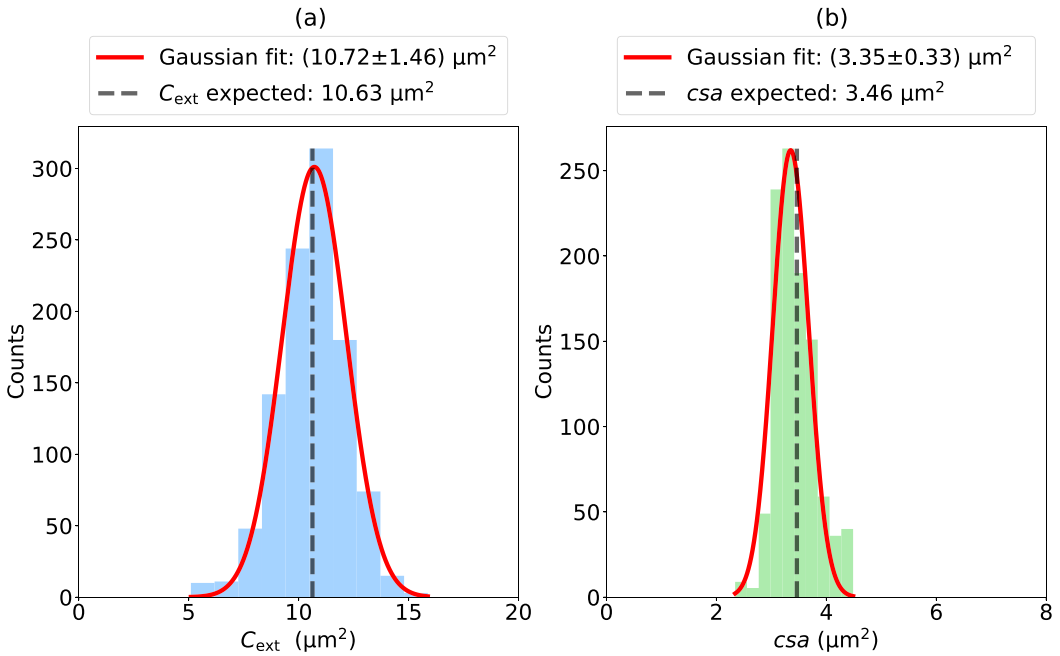

Fig. 12. (a) Extinction cross-section (C_{ext}) and (b) cross-sectional area (csa) distribution of 2.1 μm diameter polystyrene spheres in water. The Gaussian fit (red lines) are in good agreement with the expected values, shown as black dashed lines, obtained according to Mie expansion. (For interpretation of the references to color in this figure legend, the reader is referred to the web version of this article.)

suspended particles. It can be an effective tool to characterize the morphological (cross-sectional area) and optical (extinction cross-section) properties of non-spherical microparticles, such as non-soluble aerosols deposited on the cryosphere, which provide data on past atmospheric content. For example, an accurate optical characterization of mineral dust particles is crucial to retrieve robust data from the past as an input for radiative transfer models of the Earth's energy balance. The digital holography (DH) technique is being optimized to process noisy holograms in [43]. A quantitative phase analysis based on a single-shot phase unwrapping algorithm would be a considerable improvement of DH. The phase function could then be approximately associated with the height map profile of the cell, giving a 3D perspective of a cell without mechanical scanning. With a linear digital holographic system, as in our study, this task is more challenging than with an off-axis scheme. However, it is possible using for example a beam duplicator [29]. This would find useful applications in the medical field.

CRediT authorship contribution statement

Claudia Ravasio: Writing – review & editing, Writing – original draft, Visualization, Validation, Software, Methodology, Formal analysis, Conceptualization. **Luca Teruzzi:** Writing – original draft, Visualization, Validation, Software, Formal analysis. **Mirko Siano:** Writing – original draft, Validation, Methodology, Formal analysis. **Llorenç Cremonesi:** Writing – review & editing. **Bruno Paroli:** Writing – review & editing. **Marco A.C. Potenza:** Writing – review & editing, Supervision, Project administration, Conceptualization.

Declaration of competing interest

The authors declare that they have no known competing financial interests or personal relationships that could have appeared to influence the work reported in this paper.

Acknowledgments

We acknowledge Barbara Delmonte, Valter Maggi, and the entire EuroCold laboratory team for providing the snow samples. We also thank Federico Pezzotta and the staff of the machine shop of the Physics Department of the Università degli Studi di Milano for the 3D-printed design files. This research did not receive any grant from funding agencies in the public, commercial, or not-for-profit sectors.

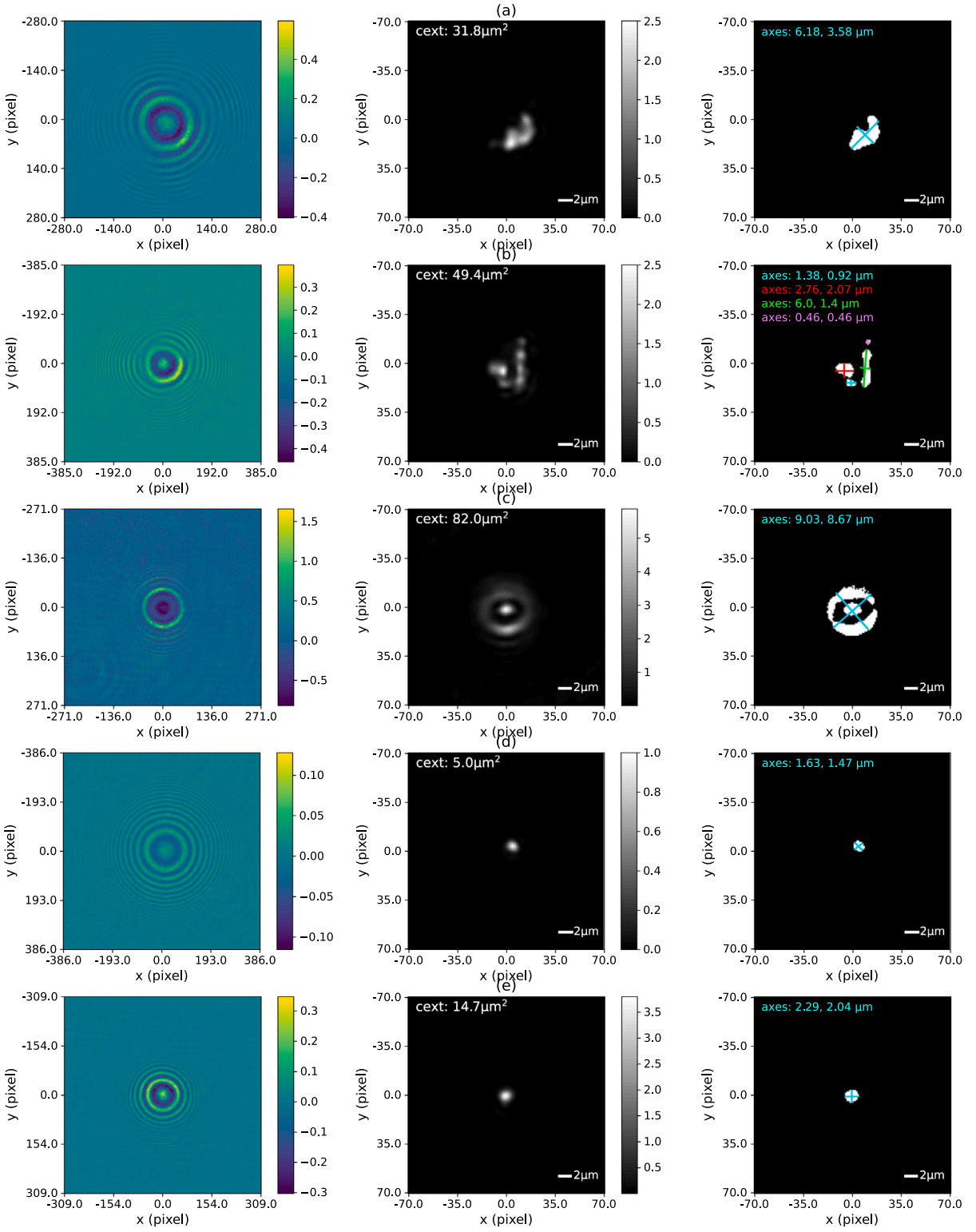

Fig. 13. Holograms and relative reconstructed images of some mineral dust relating to ice cores sample from Rutor Glacier, 2500 m - Aosta Valley, Italy. Panels (a) and (b) show dust in an aggregated form. Panel (c) shows a coarse particle with a spherical shadow. Panels (d) and (e) show fine particles, but with different amplitude intensities (as can be seen from their hologram patterns).

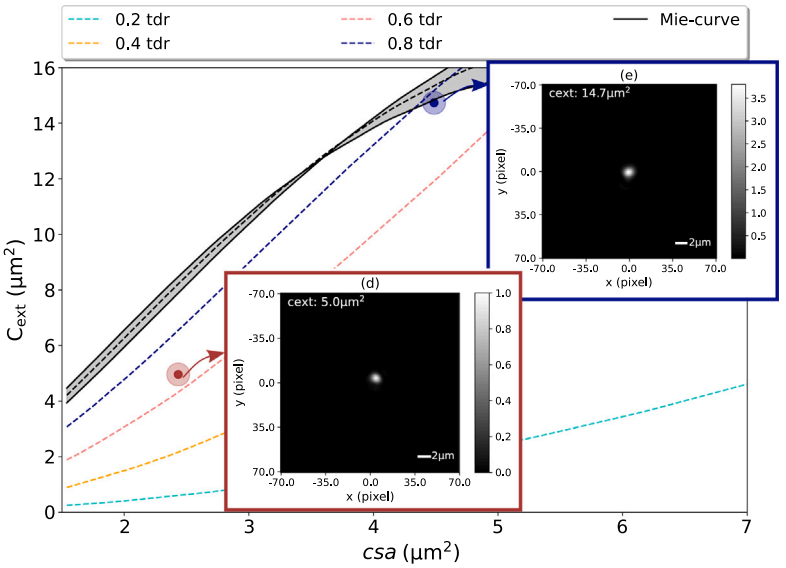

Fig. 14. (*csa*, C_{ext}) plane of particles (c) and (d) from Fig. 13. The solid black line is the Mie curve for spheres (1.15 relative refractive index), while the colored lines refer to the simulated extinction cross-section (C_{ext}) of oblate ellipsoids with a ranging thickness/diameter (*tdr*) from 0.2 (turquoise line) to 0.8 (dark-blue line). (For interpretation of the references to color in this figure legend, the reader is referred to the web version of this article.)

References

[1] S. Seebacher, Wolfgang Osten, Th Baumbach, W. Jüptner, The determination of material parameters of microcomponents using digital holography, Opt. Lasers Eng. 36 (2) (2001) 103–126.

[2] Lauren E Altman, Rushna Quddus, Fook Chiong Cheong, David G Grier, Holographic characterization and tracking of colloidal dimers in the effective-sphere approximation, Soft Matter 17 (10) (2021) 2695–2703.

[3] Antti A Aarnisalo, Jeffrey T Cheng, Michael E Ravicz, Nesim Hulli, Ellery J Harrington, Maria S Hernandez-Montes, Cosme Furlong, Saumil N Merchant, John J Rosowski, Middle ear mechanics of cartilage tympanoplasty evaluated by laser holography and vibrometry, Otol. Neurotol.: Off. Publ. Am. Otol. Soc. Am. Neurotol. Soc. Eur. Acad. Otol. Neurotol. 30 (8) (2009) 1209.

[4] Matthew J. Berg, Tutorial: Aerosol characterization with digital in-line holography, J. Aerosol Sci. (2022) 106023.

[5] Claudia Ravasio, Llorencç Cremonesi, Claudio Artoni, Barbara Delmonte, Valter Maggi, Marco AC Potenza, Optical characterization of mineral dust from the EAIIST project with digital holography, ACS Earth Space Chem. 5 (10) (2021) 2855–2864.

[6] Abid Haleem, Mohd Javaid, Ravi Pratap Singh, Rajiv Suman, Shanay Rab, Holography and its applications for industry 4.0: An overview, Internet Things Cyber-Phys. Syst. 2 (2022) 42–48.

[7] Matthew J. Berg, Nava R. Subedi, Peter A. Anderson, Measuring extinction with digital holography: nonspherical particles and experimental validation, Opt. Lett. 42 (5) (2017) 1011–1014.

[8] Heberley Tobon-Maya, Samuel Zapata-Valencia, Erick Zora-Guzmán, Carlos Buitrago-Duque, Jorge Garcia-Sucerquia, Open-source, cost-effective, portable, 3D-printed digital lensless holographic microscope, Appl. Opt. 60 (4) (2021) A205–A214.

[9] Aaron Yevick, Mark Hannel, David G. Grier, Machine-learning approach to holographic particle characterization, Opt. Express 22 (22) (2014) 26884–26890.

[10] Mikołaj Rogalski, Jose Angel Picazo-Bueno, Julianna Winnik, Piotr Zdańkowski, Vicente Micó, Maciej Trusiak, Accurate automatic object 4D tracking in digital in-line holographic microscopy based on computationally rendered dark fields, Sci. Rep. 12 (1) (2022) 12909.

[11] Eugene Serabyn, Kurt Liewer, Chris Lindensmith, Kent Wallace, Jay Nadeau, Compact, lensless digital holographic microscope for remote microbiology, Opt. Express 24 (25) (2016) 28540–28548.

[12] Lisa Dixon, Fook Chiong Cheong, David G. Grier, Holographic particle-streak velocimetry, Opt. Express 19 (5) (2011) 4393–4398.

[13] Parameswaran Hariharan, Basics of Holography, Cambridge University Press, 2002.

[14] Michael J. O'Brien, David G. Grier, Above and beyond: holographic tracking of axial displacements in holographic optical tweezers, Opt. Express 27 (18) (2019) 25375–25383.

[15] Wenbo Xu, M.H. Jericho, I.A. Meinertzhagen, H.J. Kreuzer, Digital in-line holography for biological applications, Proc. Natl. Acad. Sci. 98 (20) (2001) 11301–11305.

[16] Ulf Schnars, Claas Falldorf, John Watson, Werner Jüptner, Ulf Schnars, Claas Falldorf, John Watson, Werner Jüptner, Digital holographic particle sizing and microscopy, in: Digital Holography and Wavefront Sensing: Principles, Techniques and Applications, Springer, 2015, pp. 95–119.

[17] Dennis Gabor, A new microscopic principle, Nature 161 (1948) 777–778.

[18] Nicolas Verrier, Michael Atlan, Off-axis digital hologram reconstruction: some practical considerations, Appl. Opt. 50 (34) (2011) H136–H146.

[19] Christopher J Mann, Lingfeng Yu, Chun-Min Lo, Myung K Kim, High-resolution quantitative phase-contrast microscopy by digital holography, Opt. Express 13 (22) (2005) 8693–8698.

[20] Myungjun Lee, Oguzhan Yaglidere, Aydogan Ozcan, Field-portable reflection and transmission microscopy based on lensless holography, Biomed. Opt. Express 2 (9) (2011) 2721–2730.

[21] Thomas Kreis, Handbook of Holographic Interferometry: Optical and Digital Methods, John Wiley & Sons, 2006.

[22] Thomas G Dimiduk, Ekaterina A Kosheleva, David Kaz, Ryan McGorty, Emily J Gardel, Vinothan N Manoharan, A simple, inexpensive holographic microscope, in: Biomedical Optics, Optica Publishing Group, 2010, p. JMA38.

[23] Stephan Amann, Max von Witzleben, Stefan Breuer, 3D-printable portable open-source platform for low-cost lens-less holographic cellular imaging, Sci. Rep. 9 (1) (2019) 11260.

[24] Onur Mudanyali, Derek Tseng, Chulwoo Oh, Serhan O Isikman, Ikbal Sencan, Waheb Bishara, Cetin Oztoprak, Sungkyu Seo, Bahar Khademhosseini, Aydogan Ozcan, Compact, light-weight and cost-effective microscope based on lensless incoherent holography for telemedicine applications, Lab Chip 10 (11) (2010) 1417–1428.
[25] Jose Angel Picazo-Bueno, Karina Trindade, Martin Sanz, Vicente Micó, Design, calibration, and application of a robust, cost-effective, and high-resolution lensless holographic microscope, Sensors 22 (2) (2022) 553.
[26] Marco A.C. Potenza, Llorenç Cremonesi, An overview of the optical characterization of free microparticles and their radiative properties, J. Quant. Spectrosc. Radiat. Transfer (2023) 108773.
[27] James Hansen, Larissa Nazarenko, Soot climate forcing via snow and ice albedos, Proc. Natl. Acad. Sci. 101 (2) (2004) 423–428.
[28] S Albani, NM Mahowald, AT Perry, RA Scanza, CS Zender, NG Heavens, V Maggi, JF Kok, BL Otto-Bliesner, Improved dust representation in the community atmosphere model, J. Adv. Modelling Earth Syst. 6 (3) (2014) 541–570.
[29] A. Anand, V. Chhaniwal, B. Javidi, Tutorial: common path self-referencing digital holographic microscopy, APL Photonics 3 (7) (2018).
[30] Jorge Garcia-Sucerquia, Wenbo Xu, Stephan K Jericho, Peter Klages, Manfred H Jericho, H Jürgen Kreuzer, Digital in-line holographic microscopy, Appl. Opt. 45 (5) (2006) 836–850.
[31] Tatiana Latychevskaia, Hans-Werner Fink, Practical algorithms for simulation and reconstruction of digital in-line holograms, Appl. Opt. 54 (9) (2015) 2424–2434.
[32] Thomas M. Kreis, Mike Adams, Werner P.O. Jüptner, Methods of digital holography: a comparison, in: Optical Inspection and Micromeasurements II, Vol. 3098, SPIE, 1997, pp. 224–233.
[33] Joseph W. Goodman, Introduction to Fourier Optics, Roberts & Co Publishers, Englewood, Colorado, 2005.
[34] Pierre-Alexandre Blanche, Optical Holography: Materials, Theory and Applications, Elsevier, 2019.
[35] Solomon Barkley, Thomas G Dimiduk, Jerome Fung, David M Kaz, Vinothan N Manoharan, Ryan McGorty, Rebecca W Perry, Anna Wang, Holographic microscopy with python and holopy, Comput. Sci. Eng. 22 (5) (2019) 72–82.
[36] James A. Lock, Gérard Gouesbet, Generalized Lorenz–Mie theory and applications, J. Quant. Spectrosc. Radiat. Transfer 110 (11) (2009) 800–807.
[37] Hendrik Christoffel Hulst, Hendrik C. van de Hulst, Light Scattering by Small Particles, Courier Corporation, 1981.
[38] Bhaskar Jyoti Krishnatreya, David G. Grier, Fast feature identification for holographic tracking: The orientation alignment transform, Opt. Express 22 (11) (2014) 12773–12778.
[39] Philip Benzie, Thomas Kreis, handbook of holographic interferometry: Optical and digital methods, wiley-VCH (2005) ISBN 3-527-40546-1 preface: 2pp., main body: 408pp., appendix: 453pp.,€ 169 or£ 114, Opt. Lasers Eng. 46 (1) (2008) 94–95.
[40] Gang Pan, Hui Meng, Digital holography of particle fields: reconstruction by use of complex amplitude, Appl. Opt. 42 (5) (2003) 827–833.
[41] Weidong Yang, Alexander B. Kostinski, Raymond A. Shaw, Depth-of-focus reduction for digital in-line holography of particle fields, Opt. Lett. 30 (11) (2005) 1303–1305.
[42] Matthew J Berg, Nava R Subedi, Peter A Anderson, Nicholas B Fowler, Using holography to measure extinction, Opt. Lett. 39 (13) (2014) 3993–3996.
[43] Matthew J. Berg, Killian Aleau, Romain Ceolato, Measuring extinction with digital holography: noisy holograms, Opt. Express 31 (26) (2023) 43213–43223.
[44] M. Siano, B. Paroli, M.A.C. Potenza, Heterodyne near field speckles: from laser light to X-rays, Adv. Phys.: X 6 (1) (2021) 1891001, arXiv:https://doi.org/10.1080/23746149.2021.1891001.
[45] M. Giglio, M. Carpineti, A. Vailati, Space intensity correlations in the near field of the scattered light: A direct measurement of the density correlation function $g(r)$, Phys. Rev. Lett. 85 (2000) 1416–1419.
[46] M.D. Alaimo, D. Magatti, F. Ferri, M.A.C. Potenza, Heterodyne speckle velocimetry, Appl. Phys. Lett. 88 (19) (2006) 191101, arXiv:https://pubs.aip.org/aip/apl/article-pdf/doi/10.1063/1.2200396/14659026/191101_1_online.pdf.
[47] C. Ravasio, A digital holographic technique for studying mineral dust content in snow and ice cores, Il Nuovo Cimento C 45 (6) (2022) 1–4.
[48] Llorenç Cremonesi, Mirko Siano, Bruno Paroli, Marco AC Potenza, Near field scattering for samples under forced flow, Rev. Sci. Instrum. 91 (7) (2020) 075108.
[49] Ina Tegen, K. Schepanski, The global distribution of mineral dust, in: IOP Conference Series: Earth and Environmental Science, Vol. 7, IOP Publishing, 2009, 012001.
[50] Theo M Jenk, Sönke Szidat, Margit Schwikowski, Heinz W Gäggeler, Sabina Brütsch, Lukas Wacker, H-A Synal, M Saurer, Radiocarbon analysis in an alpine ice core: record of anthropogenic and biogenic contributions to carbonaceous aerosols in the past (1650–1940), Atmos. Chem. Phys. 6 (12) (2006) 5381–5390.
[51] Ronald W. Hoham, Daniel Remias, Snow and glacial algae: a review1, J. Phycol. 56 (2) (2020) 264–282.
[52] B Di Mauro, R Garzonio, G Baccolo, A Franzetti, F Pittino, B Leoni, D Remias, R Colombo, M Rossini, Glacier algae foster ice-albedo feedback in the European Alps, Sci. Rep.-Uk, 10 (2020) 4739.
[53] B Di Mauro, R Garzonio, C Ravasio, V Orlandi, G Baccolo, S Gilardoni, D Remias, B Leoni, M Rossini, R Colombo, Combined effect of algae and dust on snow spectral and broadband albedo, J. Quant. Spectrosc. Radiat. Transfer (2024) 108906.
[54] Ye Pu, Hui Meng, Intrinsic aberrations due to mie scattering in particle holography, J. Opt. Soc. Amer. A 20 (10) (2003) 1920–1932.
[55] Maxim A. Yurkin, Alfons G. Hoekstra, The discrete-dipole-approximation code ADDA: capabilities and known limitations, J. Quant. Spectrosc. Radiat. Transfer 112 (13) (2011) 2234–2247.

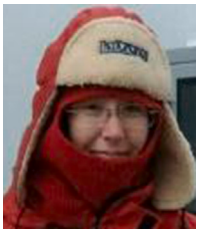

Claudia Ravasio My research focuses on the estimation of snow and ice parameters using ground-based and satellite remote sensing. I also study contaminants such as dust and algae in snow and ice cores. I am interested in assessing the environmental components of the cryosphere and the changes they are undergoing. I am familiar with radiative transfer models to estimate parameters such as water content and the presence of impurities in the snowpack. I developed algorithms to analyze data from campaigns of data collection of snow parameters, with reflectance and temperature measurements, with good feedback. I applied innovative optical techniques to the characterization of particles in ice and snow such as digital holography, light scattering, and iperspectral imaging. Field activities include the analysis of satellite images (PRecursore IperSpettrale della Missione Applicativa, PRISMA) and their comparison with ground measurements for validation and calibration of the space mission.